

Numerical Investigation of Multistage Viscous Micropump Configurations

M. Abdelgawad

I. Hassan¹

e-mail: Hassan@me.concordia.ca

N. Esmail

P. Phutthavong

Department of Mechanical and Industrial
Engineering, Concordia University, Montreal,
QC, Canada, H3G 1M8

The viscous micropump consists of a cylinder placed eccentrically inside a microchannel, where the rotor axis is perpendicular to the channel axis. When the cylinder rotates, a net force is transferred to the fluid because of the unequal shear stresses on the upper and lower surfaces of the rotor. Consequently, this causes the surrounding fluid in the channel to displace toward the microchannel outlet. The simplicity of the viscous micropump renders it ideal for micropumping; however, previous studies have shown that its performance is still less than what is required for various applications. The performance of the viscous micropump, in terms of flow rate and pressure capabilities, may be enhanced by implementing more than one rotor into the configuration either horizontally or vertically oriented relative to each other. This is analogous to connecting multiple pumps in parallel or in series. The present study will numerically investigate the performance of various configurations of the viscous micropumps with multiple rotors, namely, the dual-horizontal rotor, triple-horizontal rotor, symmetrical dual-vertical rotor, and eight-shaped dual-vertical rotor. The development of drag-and-lift forces with time, as well as the viscous resisting torque on the cylinders were studied. In addition, the corresponding drag, lift, and moment coefficients were calculated. The flow pattern and pressure distribution on the cylinders' surfaces are also included in the study. Results show that the symmetrical dual-vertical rotor configuration yields the best efficiency and generates the highest flow rate. The steady-state performance of the single-stage micropump was compared to the available experimental and numerical data and found to be in very good agreement. This work provides a foundation for future research on the subject of fluid phenomena in viscous micropumps. [DOI: 10.1115/1.1949639]

Keywords: Multiple Rotor, Viscous Micropump, CFD Simulation, MEMS

1 Introduction

Micropumps are among the most promising microelectromechanical systems (MEMS) and are ready to be implemented into many industrial applications. Micropumps operate on principles far different from those applied to conventional-sized micropumps. Because of the microscopic dimensions of the pump and its large surface-to-volume ratio, viscous forces dominate over centrifugal and viscous forces [1]. Positive displacement micropumps are most common, however, they require check valves at the inlet and outlet, thus complicating their design [1]. Stemme and Stemme [2] suggested replacing the check valves with a nozzle at the inlet and a diffuser at the outlet; however, the idea was not practical since very specific operating conditions were required in order for the pump to operate correctly. Electrohydrodynamic pumps were also proposed, where an electric field passes through the working fluid, which is a dielectric fluid. As a result, the induced charges within the fluid cause the fluid to displace, thus generating flow [3]. On the other hand, electrokinetic pumps use the moving electric field to displace ions of the electric double layer, rather than the charges in a dielectric fluid, in order to generate flow [4]. Lastly, sequential generation of thermal bubbles was also proposed, where one bubble is generated by the means of a microelectric heater to serve as a check valve, and is followed by another bubble, which is generated by another heater and

growing in the opposite direction of the first bubble. As a result, fluid is pumped in the desired direction, and the process is repeated once again [5].

The viscous micropump, first introduced by Sen et al. [1], incorporates both applicability at the microscale and simplicity in design. The viscous micropump is simply a cylinder placed eccentrically inside a channel with its axis perpendicular to the channel axis. When the cylinder rotates, a net force is transferred to the fluid due to the unequal shear rates on the upper and lower surfaces of the cylinder, thus forcing the fluid to displace. Its operation depends mainly on viscous forces, and it can operate in any situation where viscous forces are dominant. This situation would exist for either low-viscosity liquids in micropassages, due to the high surface-to-volume ratio characteristic of MEMS, or for highly viscous liquids, such as heavy polymers, in macroducts. Sen et al. [1] performed an experiment to test the pump performance. The study focused on the effect of the channel height, rotor eccentricity, and angular velocity on the pump performance and on the fluid bulk velocity in the duct.

In a later study, the same research team performed a numerical simulation of the viscous micropump solving Navier-Stokes equations for the case of the cylindrical rotor [6]. Critical values for optimum performance were calculated. The highest bulk velocity was achieved when the spacing between the plates is around one and one-half times the cylinder diameter for a fixed eccentricity or at the maximum eccentricity for a fixed plate spacing. The load-flow rate curve for the pump was also plotted, with part of the curve in the negative part of the flow-rate axis. This showed that the flow would change direction if the load were increased beyond the pump's capability. The maximum efficiency of the pump was determined to be ~2.5% for the optimum plate spacing. However, it was observed that the viscous dissipation might cause a mea-

¹Author to whom correspondence should be addressed.

Contributed by the Fluids Engineering Division for publication in the JOURNAL OF FLUIDS ENGINEERING. Manuscript received by the Fluids of Engineering Division on January 6, 2004; Final manuscript received March 10, 2005. Associate Editor: Kenneth Brauer.

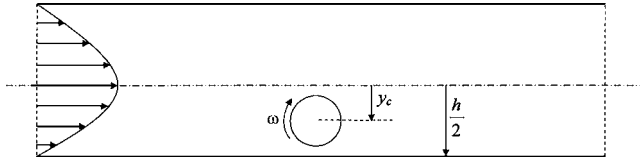


Fig. 1 Schematic of the micropump geometry for the single rotor [9]

surable temperature rise since viscous forces are the driving forces. In order to check the effect of viscous dissipation on pump performance, the same team performed a second numerical simulation [7]. In this study, they solved the continuity equation, the momentum equation with temperature-dependent viscosity, and the energy equation with viscous dissipation terms retained, all coupled together. It was determined that viscous dissipation would not cause a measurable rise in the bulk temperature of the fluid in MEMS applications, yet it may cause a significant rise in the fluid temperature combined with steep temperature gradients near the rotor where the shear stresses are maximum. Decourtye et al. [8] introduced the effects of the sidewalls of the channel in their study. As expected, the pump performance decreased in terms of bulk velocity, yet pumping action existed even for channel widths less than the rotor diameter. It was observed that the sidewall effect reduces the channel height corresponding to maximum bulk velocity and also increases the back pressure at which backflow occurs.

The transient performance of a single-rotor viscous micropump was investigated by Abdelgawad et al. [9]. The effect of the microchannel height, rotor eccentricity, Reynolds number, and pump load on the transient performance of the single-rotor viscous micropump was studied in detail. The rotor eccentricity was determined to be the parameter that affected the transient performance of the micropump most significantly. The steady-state performance was compared to the available experimental data and found to be in very good agreement.

The present study is an extension of the work conducted by Abdelgawad et al. [9] and is aimed at studying the transient and steady-state performance of multistage viscous micropumps where more than one rotor is used in order to enhance the performance. The addition of rotors is expected to improve the performance of the single-rotor viscous micropump because these rotors are essentially being placed in series or parallel inside the microchannel thus increasing the pressure rise or flow rate, respectively. More over, in some cases, the use of more than one rotor is expected to increase the pumping efficiency because of the interaction between the flow fields around all rotors which helps reduce the shear stress and, hence, the resisting torque on the rotors. Four configurations of rotors were studied in detail: the dual-horizontal rotor, triple-horizontal rotor, symmetrical dual-vertical rotor, and finally the eight-shaped dual-vertical rotor. Parameters such as average velocity, drag and moment coefficients, and efficiency will be calculated. Results obtained in [9] will be used for comparison purposes in order to determine the effect multiple rotors have on the performance of the viscous micropump. The single-rotor case used for comparison purposes was that of best pumping effect, namely, $S=1.5$, $\epsilon=0.95$, and $Re=1$.

2 Problem Geometry

2.1 Problem Configuration. The present study is a numerical investigation of multiple rotors inside a microchannel. The problem configuration for a single rotor is shown in Fig. 1, and the geometric parameters used are identical to those defined by Abdelgawad et al. [9]. The main geometrical parameters in the study will be the channel height (S), defined as

$$S = \frac{h}{d} \quad (1)$$

and the rotor eccentricity ϵ , which indicates the rotor position inside the channel, defined as

$$\epsilon = \frac{y_c}{\frac{h}{2} - \frac{d}{2}} \quad (2)$$

Based on this definition, $\epsilon=0$ corresponds to the rotor being centered on the channel axis and $\epsilon=1$ corresponds to the rotor touching the lower wall. The rotor is forced to rotate with an angular velocity ω . In this problem, the Reynolds number will be based on the rotor velocity at its surface $U=\omega d/2$ since the average velocity in the channel $\bar{u}=(1/h)\int_0^h u \, dy$ is an output of the solution. Therefore, the Reynolds number will be defined as

$$Re = \frac{Ud}{\nu} = \frac{\omega d^2}{2\nu} \quad (3)$$

The pressure is specified on the inlet and outlet of the channel, where a higher pressure is specified at the outlet. The nondimensional pressure rise is defined as

$$\Delta P^* = \frac{P_{out} - P_{in}}{\frac{\rho \nu^2}{d^2}}, \quad (4)$$

where P_{out} is the pressure on the channel outlet and P_{in} is the pressure on the channel inlet, ρ is the fluid density, and ν is the fluid kinematic viscosity. The scale used to nondimensionalize the time in the simulation was chosen to be the time taken by the rotor to finish one complete revolution

$$t^* = \frac{t}{\frac{2\pi}{\omega}} = \frac{t\omega}{2\pi} \quad (5)$$

According to this definition, the nondimensional time is simply the number of revolutions of the rotor. This provides an easier tracking of the changes in the flow field over time regardless of the rotor angular velocity. The drag and moment coefficients are defined as

$$C_D = \frac{F_D}{\frac{1}{2}\rho U^2 d} \quad (6)$$

and

$$C_M = \frac{M}{\frac{1}{2}\rho U^2 d^2} \quad (7)$$

where U is the cylinder surface velocity defined before.

2.2 Mathematical Modeling and Boundary Conditions. The two-dimensional 2D Navier-Stokes equations will be solved for the specified geometry where all the dimensions will be normalized by the rotor diameter d .

The continuity equation is

$$\nabla \cdot \vec{V} = 0 \quad (8)$$

and the momentum equation is

$$\rho \left[\frac{\partial \vec{V}}{\partial t} + (\vec{V} \cdot \nabla) \vec{V} \right] = \rho \vec{\alpha} - \nabla P + \mu \nabla^2 \vec{V} \quad (9)$$

where α represents the body forces per unit mass. Based on the above-mentioned method for nondimensionalizing and assuming that the flow is incompressible with neglected body forces, the momentum equation becomes

$$\frac{\rho\omega^2 d}{4} \left[\frac{1}{\pi} \frac{\partial \vec{V}^*}{\partial t^*} + (\vec{V}^* \cdot \nabla) \vec{V}^* \right] = \frac{\mu\omega}{2d} \vec{V}^* - \frac{\mu^2}{\rho d^3} \nabla P^* \quad (10)$$

which, in nondimensional terms, become

$$\frac{1}{\pi} \frac{\partial \vec{V}^*}{\partial t^*} + (\vec{V}^* \cdot \nabla) \vec{V}^* = \frac{1}{\text{Re}} \nabla^2 \vec{V}^* - \frac{1}{\text{Re}^2} \nabla P^* \quad (11)$$

The main independent parameters in the solution will be the channel height S , the rotor eccentricity ϵ , Reynolds number Re , and the pressure load ΔP^* . When additional rotors are added, new geometrical independent parameters will arise and their effect will be studied. These new parameters will be mentioned and defined in the corresponding sections. The flow will be assumed laminar, incompressible, and unsteady, and the fluid itself is considered Newtonian with constant properties. No-slip, no-penetration boundary conditions are assumed on the microchannel walls, and the fluid velocity is zero on the upper and lower walls and equal to the rotor surface velocity on the rotor boundary. The pressure is specified on the inlet and outlet of the microchannel. Pressure will be always assumed to be zero gage pressure at the inlet, and its value at the exit will be varied to simulate different loads. The location of the inlet and outlet were chosen to be eight diameters upstream and downstream of the microchannel vertical centerline, respectively. This distance was found to be large enough to achieve uniform flow at the inlet and outlet without being affected by the rotors existence. The fluid will be assumed to be initially at rest ($\vec{V}=0$) and the motion will start by rotating the cylinder clockwise with an angular velocity ω .

3 Numerical Modeling

The CFD package FLUENT 6.0 is used to numerically solve the Navier-Stokes equations. This CFD package uses the finite volume method and supports unstructured grids. It enables the use of different discretization schemes and solution algorithms, together with various types of boundary conditions. As part of the same package, a preprocessor, GAMBIT, is used to generate the required grid for the solver. An unstructured grid with triangular elements is used. The cylinder surface was divided into 100 equally spaced elements. The upper and lower walls were divided into 200 non-uniformly spaced elements using the bell-shaped meshing scheme with a ratio $R=0.4$. The grid was finer in regions near the center and adjacent to the cylinder and coarser in regions far upstream and downstream. The bell-shaped scheme meshes the edge so that the node distribution follows a normal distribution curve centered at the geometric center of the edge. The ratio R specifies whether the nodes will be denser at the center of the edge or at its ends and also specifies the intensity of this distribution. In addition to this meshing method, which refines the grid in the cylinder region, grid adaptation by the solver itself was performed in the gap between the cylinder and the lower wall for cases of high eccentricities, where this gap size is very small. The PISO-SIMPLE algorithm, where PISO stands for pressure-implicit with splitting of operators, was used for the pressure-velocity coupling. It is nearly the same as the SIMPLE algorithm, presented in [10], except that it takes into account two additional corrections. The first one is the neighbor correction. This correction incorporates more iterations into the pressure correction equation in order to satisfy the continuity and momentum equations more precisely. Thus, the PISO algorithm requires more time per iteration, but at the same time reduces the total number of iterations. Therefore, the total time is much less, rendering it more suitable for transient applications. The second correction is the skewness correction, which simply enables the solver to deal with highly skewed meshes and reduce the total number of iterations required for the convergence of such meshes.

Two different discretization schemes were used for the time and momentum equations. A power-law scheme was used for the two momentum equations, whereas a second-order discretization scheme was used for the time derivatives. Under relaxation was

used during the solution with the underrelaxation factors varying between 0.3 and 1 to ensure convergence. Multigrid methods were also used in order to reduce convergence time. The use of multigrids helps reduce the low-frequency error components when the equations are iterated on a coarser mesh. By default, a V-cycle multigrid is chosen for the pressure correction equation, whereas a flexible cycle was chosen for momentum equations. In the V-cycle, one iteration is first performed on the finest grid to reduce the high-frequency components of the error and then the solution is restricted to the coarser grid. After a certain number of iterations on the coarser grid, the solution is interpolated to the finer grid where it is reiterated. For the flexible cycle, the use of coarse grid corrections is called only in the cases where the convergence rate on the current grid is slow.

Different meshes were used to determine the optimum grid size and to ensure grid-independent solutions. Grid-independent solution was assured by observing three parameters. The first parameter is the distribution of the x -velocity component on a vertical plane just one diameter from the cylinder axis, which will indicate whether the grid is fine enough in the neighborhood of the cylinder where the largest shear stresses exist. The second parameter is the change of the drag coefficient of the cylinder with time, which tests the coupling between the grid size and the time step chosen. The convergence of the drag coefficient over the grid size was achieved on the third mesh used. The trend of the drag coefficient variation with time on all the meshes used was the same, where differences only occurred between the coefficient values themselves. This was also the case for the x -velocity distribution. The third parameter is the average velocity of the flow at the outlet of the microchannel, which will give a good indication of the effect of the grid size in the entire microchannel domain. As a convergence criterion in the present work, the solver iterated the equations until the scaled residuals are less than 10^{-5} or until it stabilized at a constant value, which is still small enough to ensure convergence. This value varied approximately from 10^{-5} to 3×10^{-4} , based on the parameters for each specific case. The time step used for simulating the transient behavior of the flow needed to be small enough to pick the physical changes over time inside the flow field, as well as to ensure stability. Different time steps were tested at the beginning in order to determine the optimum time step to be used. Obviously, the optimum time step size varies from one case to another, since the Reynolds number (i.e., the cylinder angular velocity) is different in the various cases. The optimum time step should be the one that, when coupled with the cylinder angular velocity, corresponds to small changes in the cylinder angular displacement so that any changes in the flow field that result from this angular displacement may be monitored. The change of the average velocity inside the microchannel with time was used as a criterion to determine the optimum step size. The results for $\Delta t=0.0001, 0.001, \text{ and } 0.01 \text{ s}$ (corresponding to $\Delta t^*=32 \times 10^{-6}, 32 \times 10^{-5}, 32 \times 10^{-4}$, respectively) were nearly the same, whereas for $\Delta t=0.1 \text{ s}$ (corresponding to $\Delta t^*=32 \times 10^{-3}$), instability and large fluctuations in the average velocity occur. The time step chosen for nearly all cases studied was 0.001 s ($\Delta t^*=32 \times 10^{-5}$), which was small enough to recognize all the changes in the flow field over time, and, in addition, was large enough to achieve reasonable computation time.

4 Results and Discussion

In this section, the steady-state and transient performance of the dual-horizontal, triple-horizontal, symmetrical dual-vertical, and the eight-shaped rotors were compared to those of the single-rotor viscous micropump. Steady-state cases for the single-rotor viscous micropump were first simulated by Abdelgawad et al. [9], and the results were compared to existing experimental results obtained by Sen et al. [1] and numerical results obtained from Sharatchandra et al. [6]. The effect of the microchannel height on the flow rate was studied both experimentally and numerically in [1] and [6]. For comparison purposes, 11 cases were simulated with chan-

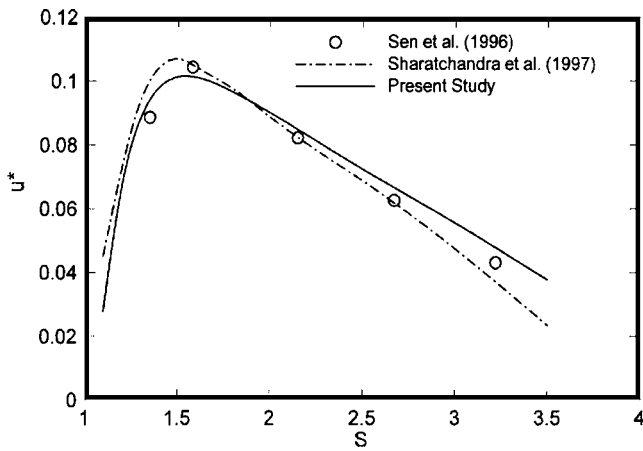


Fig. 2 Comparison of average velocity versus channel height for the single rotor ($Re=0.5, \Delta P^*=0.5$ and $\epsilon=0.9$) [9]

nel heights ranging from $S=1.1$ to 3.5 with an eccentricity $\epsilon=0.9$. In all cases studied, the Reynolds number was kept constant at $Re=0.5$ and the pressure load was held constant at $\Delta P^*=0.5$. Figure 2 shows that the results are in very good agreement with both the computational and experimental results of the previous group [1,6]. The rotor eccentricity in the microchannel is the main parameter that initiates the driving force in the microchannel. Sharatchandra et al. [6] studied the effect of the rotor eccentricity on the fluid average velocity in the channel and observed that the average velocity increases nearly linearly with the eccentricity. Figure 3 generated by Abdelgawad et al. [9] compares the results calculated by Sharatchandra et al. [6] to those calculated in the present study. Both show the linear variation of the average velocity with the rotor eccentricity.

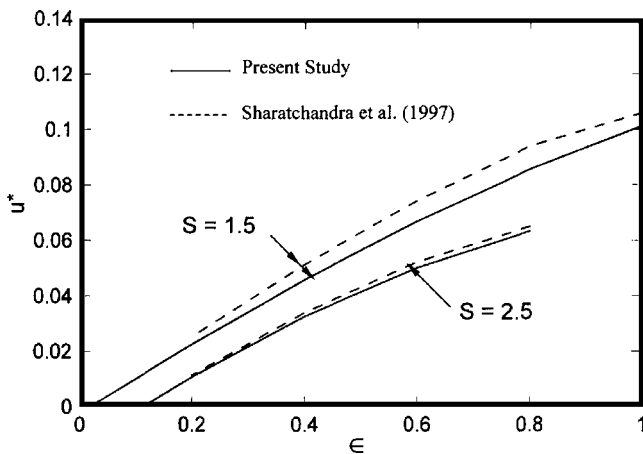


Fig. 3 Comparison of average velocity versus eccentricity at $\Delta P^*=1$ and $Re=1$ for the single rotor [9]

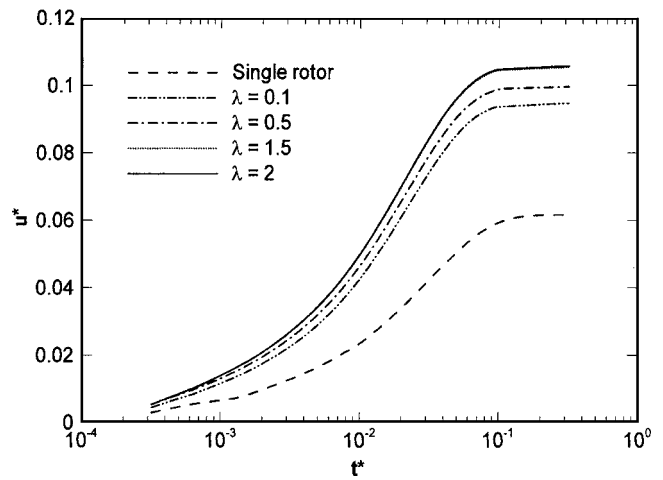


Fig. 5 Comparison of the variation of velocity with time for the dual-horizontal rotor for different rotor spacing with that for the single rotor ($S=1.5, \epsilon=0.95, \Delta P^*=10$, and $Re=1$)

4.1 Dual- and Triple-Horizontal Rotors. The mesh used to study the dual-horizontal rotor is shown in Fig. 4. The effect of the horizontal distance between the two cylinders L was studied, where it was varied between $0.1d$ and $2d$. The parameter λ was used and is defined as

$$\lambda = \frac{L}{d} \quad (12)$$

Figure 5 presents the variation of velocity with time for different rotor spacing. As expected, the flow rate for the dual rotor yields higher flow rates than that for the single rotor at the same back pressure. At all values of λ the average velocity inside the channel increases gradually until it reaches its steady-state value. The flow field inside the micropump reaches steady state within one rotor revolution in the single-rotor case and at all values of λ in the dual-rotor case. It can be observed that the flow rate increases with increasing λ until the value of $\lambda=1.5$ after which, the flow rate remains constant. At smaller values of λ , the two flow fields around both rotors interact together, thus the pumping action resulting from each rotor is not maximum. Although at $\lambda \geq 1.5$ these flow fields become independent of each other and each rotor produces its maximum pumping effect. As shown in Fig. 5, the flow rate for $\lambda=2.0$ is 1.72 times that generated in the single-rotor micropump at the specified conditions ($\Delta P^*=10$). The effect of increasing λ on the flow field is shown in Fig. 6. For small values of λ , two big vortices and a small one exist in the flow field. The two big vortices are located upstream of the upstream cylinder and downstream of the downstream cylinder. The small vortex exists between the two cylinders on the upper wall. This vortex increases in size with increasing λ until it becomes two big vortices encircled together inside a bigger vortex at $\lambda=2$.

When the development of the flow field with time is examined

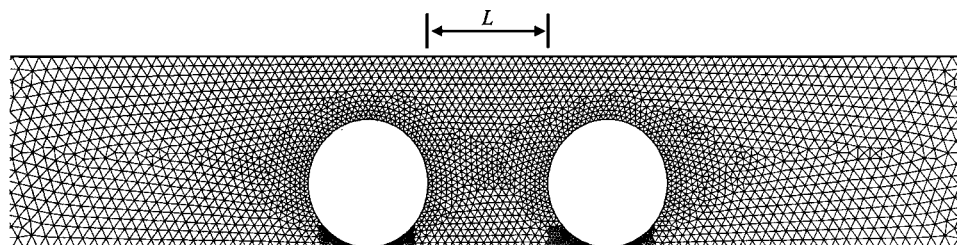


Fig. 4 Mesh used for the dual-horizontal-rotor viscous micropump

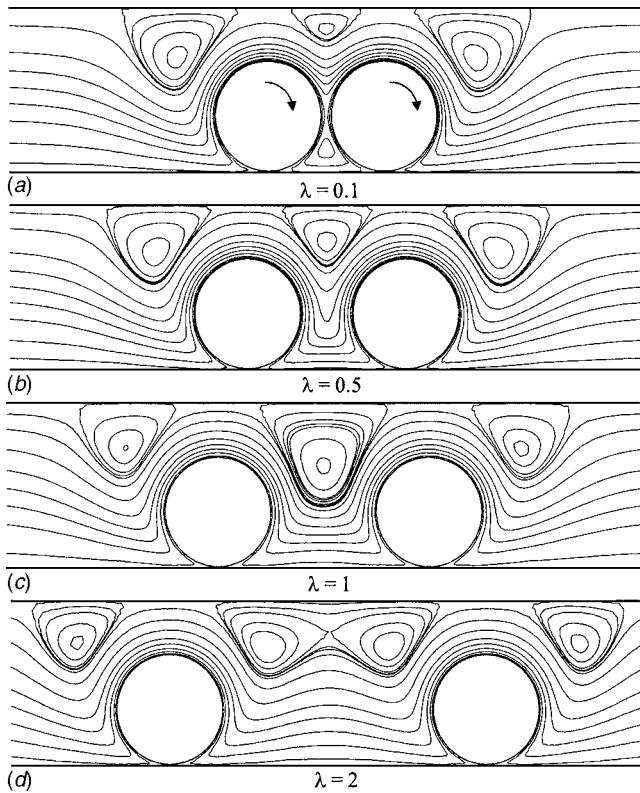


Fig. 6 Streamlines for different rotor spacing of the dual-horizontal rotor ($S=1.5, \epsilon=0.95, \Delta P^*=10$, and $Re=1$)

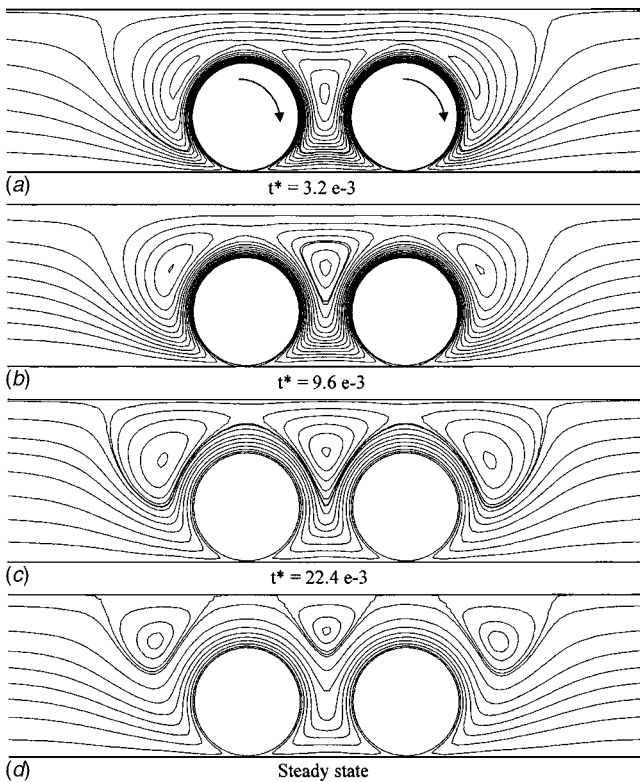


Fig. 7 Streamlines at different times at $\lambda=0.5$ for the dual-horizontal rotor ($S=1.5, \epsilon=0.95, \Delta P^*=10$, and $Re=1$)

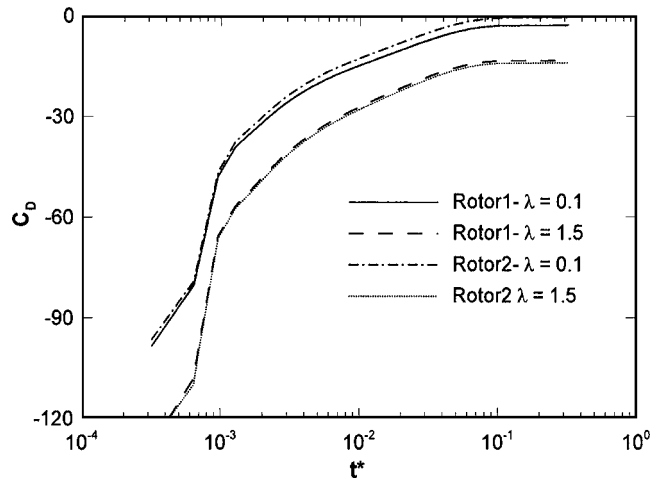


Fig. 8 Variation of the drag coefficient with time on rotors 1 and 2 for different rotor spacing of the dual-horizontal rotor ($S=1.5, \epsilon=0.95, \Delta P^*=10$, and $Re=1$)

(Fig. 7), it can be seen that all the vortices start very close to the cylinder's surface, as in the case of the single-rotor micropump. With time, all the vortices move away from the cylinders until they rest on the channel upper wall.

Figure 8 presents the variation of the drag coefficient with time in the dual-horizontal configuration for each of the rotors. The upstream rotor is designated as rotor 1 and the downstream rotor as rotor 2. The drag coefficient on both rotors is negative (i.e., to the left) as expected starting with a large value and decreases with time until it reaches its steady-state value. This behavior is a result of the high-rotor eccentricity, which means a very small gap between the rotors and the lower channel wall. This small gap makes the lower wall obstruct the vertical component of the fluid velocity forming a semi-stagnation zone, which increases the pressure on the downstream lower surface of both rotors resulting in a high drag coefficient. With time, and because of this high pressure, the fluid velocity is developed and is directed away from the wall, causing the pressure to be reduced and, consequently, the drag coefficient decreases.

The contribution of viscous forces to the drag coefficient is considerably less than that of the pressure forces. Figure 9 compares the value of the viscous drag to that of the pressure drag for the case of the single-rotor viscous micropump, which was studied in detail by the authors in [9]. Moreover, it should be noted that viscous forces on the upper and lower surfaces of the rotor are opposite in direction, so that they nearly cancel out in cases of low eccentricities. In cases of high eccentricities, such as the one in Fig. 8, the viscous stresses on the lower surface are higher than

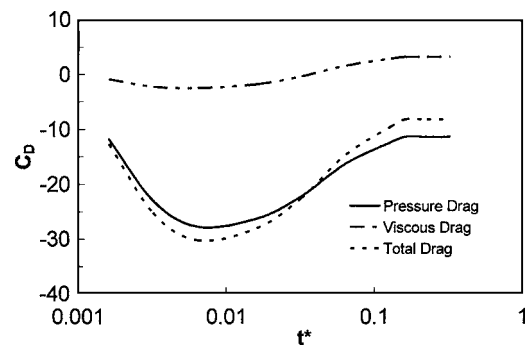


Fig. 9 Viscous, pressure, and total drag coefficients for $\epsilon=0.4$ in the single-rotor viscous micropump. ($S=1.5, \Delta P^*=0$, and $Re=1$)

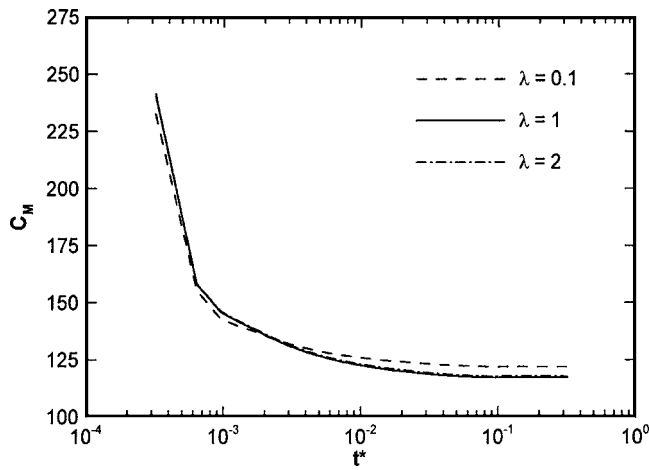


Fig. 10 Total moment coefficient at different rotor spacing of the dual-horizontal rotor ($S=1.5$, $\epsilon=0.95$, $\Delta P^*=10$, and $Re=1$)

that on the upper surface, thus the net viscous drag will be positive (i.e., to the right). Yet it will still be lower than the pressure drag, and the total drag coefficient will remain negative.

As expected, the drag coefficient curves are nearly identical at high values of λ since the flow fields are uncoupled. For smaller values of λ , slight discrepancies occur as the flow reaches steady state, where rotor 1 is subjected to higher drag than rotor 2. The drag coefficient increases on both rotors as λ is increased. This is because of the separation of the pressure fields around each rotor from each other when the rotors are farther apart. When the rotors are very close to each other, the high-pressure zone downstream of the first rotor is very close to the low-pressure zone upstream of the second rotor and so the pressure in the space between the rotors attains a moderate value. This makes the pressure drag force on each rotor less than the case when the two rotors are far from each other, with each one having a high-pressure zone on its downstream side and a low-pressure zone on its upstream side.

The moment coefficient for rotors 1 and 2 were added to yield the total moment coefficient. Its variation with time for different values of λ is shown in Fig. 10. This total moment coefficient, together with the Reynolds number, specifies the energy input to the micropump. At the beginning the moment coefficient is very high because of the very high-velocity gradients, and shear stresses, consequently, on rotors surfaces. With time, the velocity of the fluid layers adjacent to the rotors increases and the velocity gradient and shear stresses on the rotors' surfaces are reduced, causing the moment coefficient to decrease. When the effect of λ is studied, it is found that the total moment coefficient is higher at smaller values of λ because of the increase in the shear stress on the parts of cylinder surfaces facing each other. The cylinder surface velocities are moving in opposite directions in the region between the two rotors, thus increasing the velocity gradient and, hence, the shear stress on the surfaces flanking this middle region. Hence, the resisting torque and the overall moment coefficient will increase when λ is small.

The efficiency of the viscous micropump is defined as

$$\eta = \frac{\text{flow energy rise}}{\text{input mechanical energy}}$$

which, when mathematically formulated, gives the following relation:

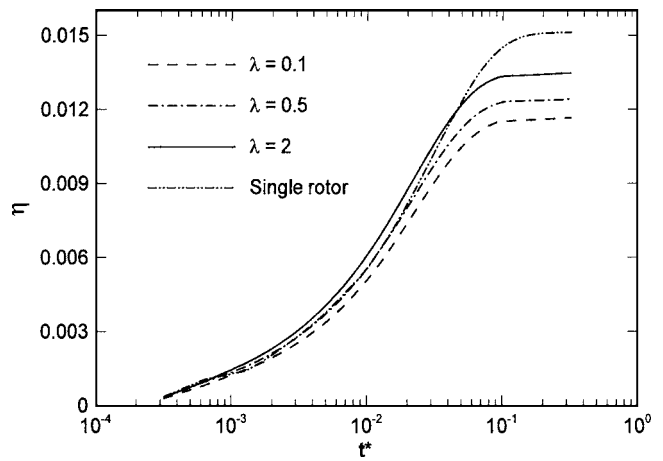


Fig. 11 Comparison of the efficiency at different rotor spacing of the dual-horizontal rotor

$$\eta = \frac{\frac{m\Delta P}{\rho}}{M\omega} = \frac{\Delta P^* u^* S}{C_M Re^2} \quad (13)$$

Based on the aforementioned information, the efficiency will be higher for higher values of λ since there will be less resisting torque, as shown in Fig. 11. However, the single rotor still has a higher efficiency since for the dual-horizontal rotor, the resisting torque is higher than that of the single rotor.

The triple-horizontal-rotor viscous micropump is the same as the dual-rotor micropump except that three rotors are used (Fig. 12). The parameter λ is defined as before in Eq. (12), and its value is the same in between adjacent rotors. The behavior for the triple-horizontal rotor is similar to that of the dual-horizontal rotor. At steady state, vortices exist adjacent to the upper wall in regions between rotors (Fig. 12), as well as in the most upstream and most downstream portions of the microchannel. As λ is increased, the flow fields once again become uncoupled, and therefore the flow rate increases and the resisting torque decreases, thus increasing the efficiency. Figure 13 shows the average velocity against the back pressure for the single-, dual-, and triple-rotor viscous micropumps. The maximum allowable pressure load for the triple-horizontal configuration is three times that for the single rotor, as expected for a series arrangement of three rotors.

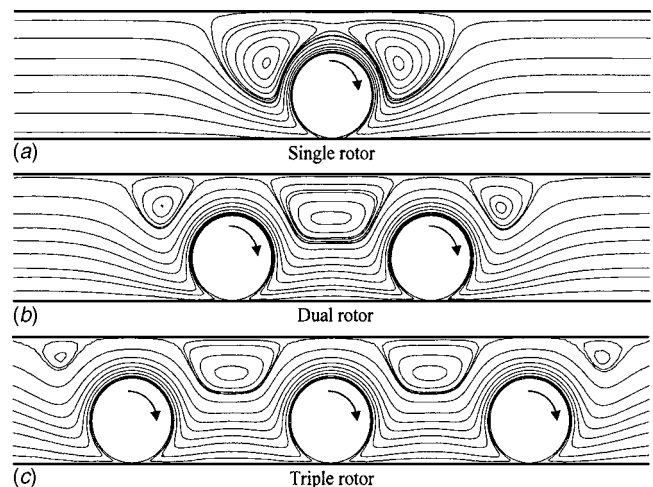


Fig. 12 Flow field around rotors in the single-rotor, dual-horizontal-rotor, and triple-horizontal-rotor viscous micropump

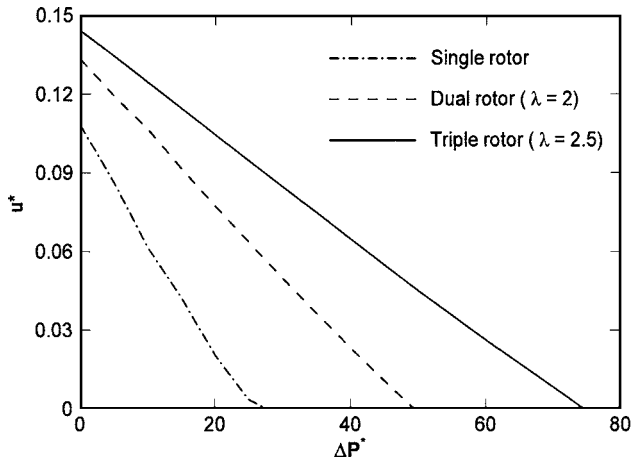


Fig. 13 Average velocity versus pressure load for the single, dual-horizontal and triple-horizontal rotors ($S=1.5$, $\epsilon=0.95$, and $Re=1$)

4.2 Symmetrical and Eight-Shaped Dual-Vertical Rotor.

The symmetrical dual rotor is a configuration in which the rotors work in parallel, as two rotors are placed above each other with each rotor close to one of the channel walls. In the symmetrical dual-rotor viscous micropump, no new geometrical parameters were introduced. The eccentricity ϵ is still the only parameter that identifies the position of each cylinder inside the channel. Yet, it has to be mentioned that in the symmetrical dual rotor configuration, the eccentricity of each cylinder is calculated separate from the other one and, based on the value of (S), equals half the actual channel height. This configuration is expected to be very efficient since one of its characteristics is the reduction of the shear stress, and hence the resisting torque, on both rotors.

Figure 14 shows the variation of the flow pattern with time for the symmetrical dual-vertical rotor. The flow pattern is symmetrical about the centerline of the channel, where the flow pattern of a single rotor is mirrored about the line of symmetry. The main advantage of the dual-symmetrical-rotor configuration of the viscous micropump is that it permits a higher velocities at the centerline of the channel compared to a zero velocity restriction on the upper wall if the upper half of the micropump did not exist. This directly increases the flow rate pumped for the same shear level (i.e., the same rotor speed). Moreover, permitting the velocity to be maximum at the centerline reduces the velocity gradient and viscous shear stress on the rotor's inward surfaces, which reduces the required torque and increases the pumping efficiency. Another consequence of the fluid velocity being highest at the centerline is the reduction in the size of the upstream and downstream vortices above each rotor, as shown in Fig. 14(c).

Figure 15 compares the variation of the average velocity at the outlet with time for the single rotor and the symmetrical dual-vertical rotor at two different eccentricities for $\Delta P^*=10$. The symmetrical dual-vertical rotor is capable of overcoming the back pressure, and therefore the velocity remains positive until steady state is attained. It must be noted that for the same average velocity, the symmetrical dual-vertical rotor will deliver a higher flow rate than the single-rotor viscous micropump because the channel height is doubled for the first one. For the symmetrical dual-vertical-rotor micropump, higher eccentricities still yield higher average velocities, as is the case for the single-rotor micropump [9].

In the eight-shaped dual-vertical-rotor micropump, two cylinders rotating clockwise were placed together, one on top of the other, to form the shape of number eight. This eight-shaped rotor was placed near the lower wall. This configuration was not expected to improve the performance of the viscous micropump, yet it was investigated to expand the knowledge of the viscous micro-

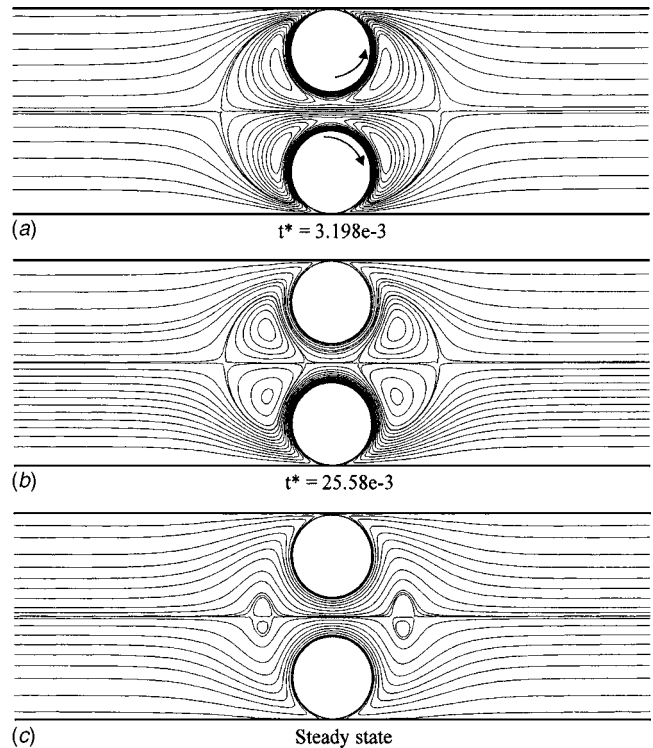


Fig. 14 Variation of the streamlines for the symmetrical dual-vertical-rotor viscous micropump with time ($S=2.5$, $\epsilon=0.95$, $\Delta P^*=10$, and $Re=1$)

pump, as well as for comparison purposes. Figure 16 shows the streamlines for this configuration at channel heights $S=2.5$ and $S=3$. It is clear that at $S=3$, the pump is unable to sustain a net flow against a pressure of $\Delta P^*=10$, which is not relatively high, thus a back flow occurs and the flow passes from right to left in the passage between the upper wall and the big vortex around the two cylinders. In such a geometrical configuration, it is expected to have a higher resisting torque on the lower rotor because of its position between the lower wall and the upper rotor. This position helps increase the velocity gradient and consequently, the shear stress on its lower and upper surfaces.

Figure 17 compares the shear stress distribution on the upper and lower rotors of the eight-shaped rotor to the shear stress on

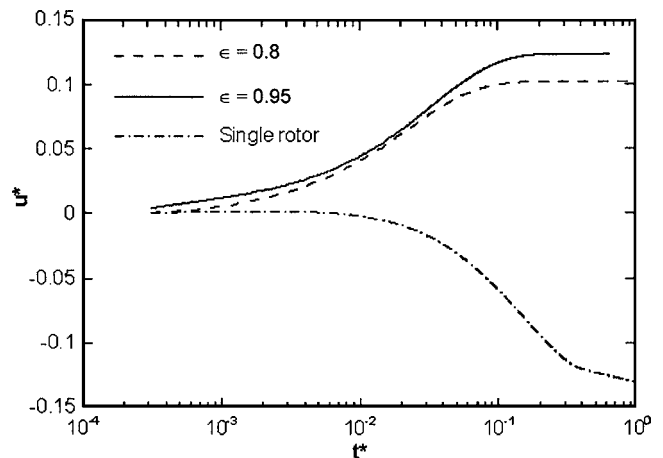


Fig. 15 Comparison of the variation of the average velocity with time for the symmetrical dual-vertical rotor with that for the single rotor ($S=2.5$, $\epsilon=0.95$, and $Re=1$)

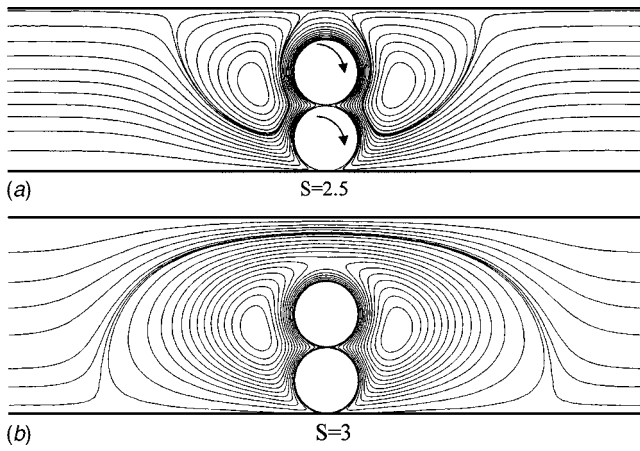


Fig. 16 Streamlines in the eight-shaped dual-vertical-rotor micropump for different S ($\epsilon=0.95, \Delta P^*=10$, and $Re=1$)

the single rotor. It is very clear from the figure that the shear stress is higher on the lower rotor than on the upper rotor and both are higher than the shear stress on the single rotor. It should be noted that the eccentricity is based on half the channel height and, therefore, the eccentricity based on the entire channel height is greater than 0.95. This accounts, partially, for the higher values of shear stress for the eight-shaped rotor. The increase in the shear stress on the lower rotor will certainly increase its moment coefficient more than it is on the upper rotor. This is confirmed by Fig. 18, which compares the moment coefficient on both rotors to that of the single rotor.

In order to determine which configuration for the multistage viscous micropump yields the best performance, the variation of the volumetric flow rate with the pressure load (Fig. 19), as well as the variation of the efficiency with time (Fig. 20) for all configurations were plotted. In Fig. 19, it was observed that the performance of the eight-shaped rotor is almost identical to that of a single rotor. The triple-horizontal rotor can withstand the highest-pressure load; however, the volumetric flow rate is not very high with values similar to that generated by the single rotor. The best compromise is the symmetrical dual-vertical rotor because it yields the highest flow rate and is also able to accommodate higher-pressure loads. Figure 20 gives final confirmation that the symmetrical dual-viscous rotor is superior to all others. The efficiency is much higher than any of the other configurations, with

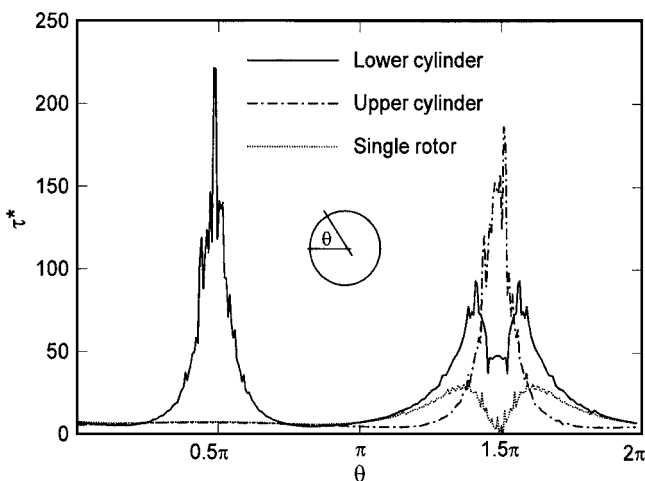


Fig. 17 Comparison of the shear stress distribution on lower and upper rotors of the eight-shaped rotor with that on the single rotor ($S=2.5, \epsilon=0.95, \Delta P^*=10$, and $Re=1$)

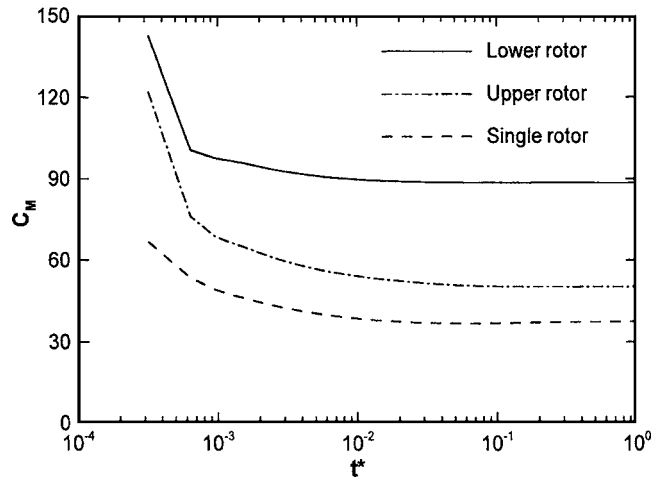


Fig. 18 Moment coefficient on lower and upper rotors compared to the single rotor ($S=2.5, \epsilon=0.95, \Delta P^*=10, Re=1$)

the eight-shaped dual-vertical rotor yielding the worst performance of them all. The second-best configuration is the dual-horizontal rotor, which is capable of withstanding higher pressure loads than that for the symmetrical dual-vertical rotor.

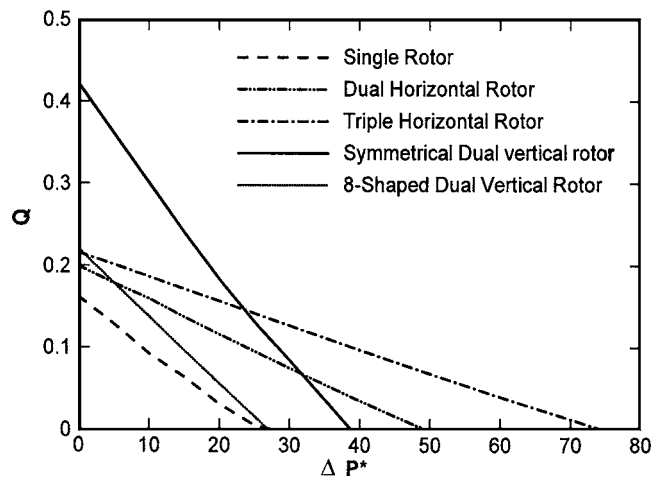


Fig. 19 Comparison of the Q - P curves of all the multistage viscous micropumps to the single-rotor viscous micropump

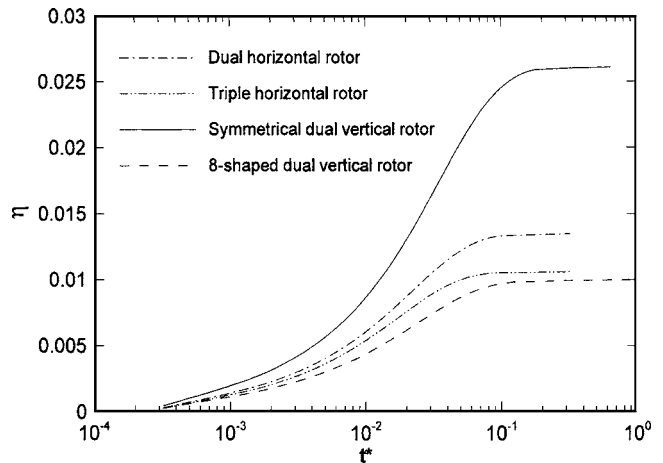


Fig. 20 Comparison of the efficiency for all the multistage viscous micropumps tested

5 Conclusions and Future Directions

Multirotor micropumps have been proven to provide flow rates and back pressures that are higher than single-rotor micropumps. They simulate the use of more than one pump, either in series or in parallel, depending on how they are placed relative to each other inside the micropump. A new geometrical parameter λ arises in the case of dual- and triple-horizontal-rotor micropumps, to account for the horizontal distance between rotors. Both the efficiency and the flow rate increase when λ increases because of the reduction in the interaction between the rotors. However, after a certain distance, the flow fields become uncoupled, there is little interaction between them, and λ has no effect on the pump performance. The dual- and triple-horizontal rotors were able to withstand higher-pressure loads than the single rotor, since the rotors are essentially placed in series.

The symmetrical dual-vertical rotor arranges two rotors in parallel. Two single-rotor flow patterns are mirrored about the centerline of the channel; thus, there is little interaction of the flow fields. The flow rate is highest of all configurations studied and able to overcome high back pressure when the single rotor could not. The efficiency is highest in this configuration because of the reduction in the shear stress and the viscous torque on both rotors.

The eight-shaped dual-vertical rotor was studied merely to further the knowledge of viscous micropumps and was not expected to improve the performance of the viscous micropump in any way. This configuration yields higher shear stress on the rotor surfaces, when compared to that on the single rotor. Consequently, there is higher viscous resistance, which hinders the performance of the micropump.

In terms of performance, the symmetrical dual-vertical-rotor micropump achieved the best efficiency and highest flow rate, while the triple-horizontal rotor achieved the highest back pressure with efficiency less than that of the single rotor. The eight-shaped dual-vertical rotor viscous micropump has the lowest efficiency with a $\Delta P^* - Q$ curve very close to that of the single-rotor micropump. In conclusion, the performance and efficiency of the viscous micropump have been increased through changing the pump geometry. This confirms the fact that there is still more to learn about it and opens the door for more research efforts to further enhance this performance and efficiency. The simplicity of the viscous micropump design and its size flexibility provides great potential for this device in commercial applications and is thus worthy of further study in the future.

Nomenclature

C_D	= cylinder drag coefficient
C_M	= cylinder moment coefficient
d	= diagonal length of rotor, m
F_D	= drag force on cylinder, N/m
h	= channel height, m
L	= distance between adjacent rotors, m

M	= moment on cylinder, N m/m
\dot{m}	= mass flow rate, kg/s
P_{in}	= inlet pressure, Pa
P_{out}	= outlet pressure, Pa
P^*	= nondimensional pressure
ΔP	= channel pressure rise, Pa
ΔP^*	= nondimensional pressure rise
Q	= nondimensional volume flow rate
Re	= Reynolds number
R	= computations residuals
S	= nondimensional channel height
t	= time, s
t^*	= nondimensional time
Δt	= time-step size, s
\bar{u}	= average velocity inside microchannel, m/s
u^*	= nondimensional average velocity
U	= cylinder surface velocity, m/s
\vec{V}	= fluid velocity vector, m/s
y_c	= distance from channel axis to cylinder center, m

Greek Letters

α	= body forces per unit mass, m/s^2
ϵ	= rotor eccentricity
λ	= nondimensional distance between adjacent rotors
μ	= fluid dynamic viscosity, Pa s
ν	= fluid kinematic viscosity, m^2/s
θ	= angle sweep over surface, rad
ρ	= fluid density, kg/m^3
τ	= fluid shear stress, Pa
τ^*	= nondimensional fluid shear stress
ω	= rotor angular velocity

References

- [1] Sen, M., Wajerski, D., and Gad-el-Hak, M., 1996, "A Novel Pump for MEMS Applications," *ASME J. Fluids Eng.* **118**, pp. 624–627.
- [2] Stemme, E., and Stemme, G., 1993, "Valveless Diffuser/Nozzle-Based Fluid Pump," *Sens. Actuators, A* **39**(2), pp. 159–167.
- [3] Bart, S. F., Tavrow, L. S., Mehregany, M., and Lang, J. H., 1990, "Microfabricated Electrohydrodynamic Pumps," *Sens. Actuators, A* **21**(1–3), pp. 193–197.
- [4] Harrison, D. J., Manz, A., and Glavina, P. G., 1991, "Electroosmotic Pumping Within a Chemical Sensor System Integrated on Silicon," *Proc. of Int. Conf. on Solid-State Sensors and Actuators Transducers*, pp. 792–795.
- [5] Kim, C. J., 2000, "Microfluidics Using the Surface Tension Force in Microscale," *Microfluidic Devices and Systems III, Proc. SPIE*, **4177**, pp. 49–55.
- [6] Sharatchandra, M. C., Sen, M., and Gad-el-Hak, M., 1997, "Navier-Stokes Simulation of a Novel Viscous Pump," *ASME J. Fluids Eng.*, **119**, pp. 372–382.
- [7] Sharatchandra, M. C., Sen, M., and Gad-el-Hak, M., 1998, "Thermal Aspects of a Novel Viscous Pump," *ASME J. Heat Transfer* **120**, pp. 99–107.
- [8] Decourtye, D., Sen, M., and Gad-el-Hak, M., 1998, "Analysis of Viscous Micropumps and Microturbines," *Int. J. Comput. Fluid Dyn.* **10**, pp. 13–25.
- [9] Abdelgawad, M., Hassan, I., and Esmail, N., 2004, "Transient Behavior of the Viscous Micropump," *Microscale Thermophys. Eng.* **8**(4), pp. 361–381.
- [10] Patankar, Suhas V., 1980, *Numerical Heat Transfer and Fluid Flow*, Taylor and Francis, New York.